

Cooling profiles of laser induced temperature fields for superconducting vanadium nitrate products

Moses Eterigho Emeteri¹

Received: 10 February 2014 / Accepted: 15 April 2015 / Published online: 1 May 2015
© Springer-Verlag Berlin Heidelberg 2015

Abstract The flexibility of vanadium nitrate makes it a good constituent for emerging superconductors. Its thermal instability engenders a disordered structure when doped by insulating constituents. The physics of the heat source i.e. the probe laser was theoretical derived to avoid deficiency of the superconducting material at low laser energy density. The mathematical experimentation was accomplished by queering the energy balance and heat conductivity of the individual constituents of the reagent. In-depth analysis of the layered distribution of laser induced temperature fields was carried out by cooling the compound via the forced convective cooling technique to about 150 °C. The material was gradual heated via the laser probe to its superconducting state. The structural defect which explained different state of the thermal outcomes were explained and proven to correspond with experimental outcomes. The temperature distribution under the irradiating laser intensity (0.45 W) shows an effective decay rate probability density function which is peculiar to the concept of photoluminescence. The dynamics of the electronic structure of thermally-excited superconducting materials is hinged on the complementary stoichiometry signatures, thermal properties amongst others. The maximum possible critical temperatures of the inter-layer were calculated to be about 206 K.

1 Introduction

The micro porosity of Vanadium nitride makes it a good candidate for microelectronics hardware. Its flexibility to allow for doping is one of its advantage for fabricating semiconductor or superconductor [1]. For example the preparation of vanadium nitride via ammonolysis of sol-gel derived $V_2O_3-SiO_2$ [2] or the optimized synthesis technique of vanadium nitride and phosphor or arsenic [3]. The disordered structure of $V_2O_3-SiO_2$ driven vanadium nitride is contrary to previous work on the high-quality poly-Si films [4–6] especially the use of excimer laser technology [7]. The accessibility or resistance of the micro porosity of vanadium nitride to thermal probe depends on the insulating matrix of dopant (see Fig. 1 below). However, the thermal probe source cannot be under-estimated because vanadium nitrate (VN) possesses high temperature durability. The prospects of the laser technology had been challenged with the alteration of chemical compounds [8]—leading to ion damage of films [9]. In recent time, the rudiments of the laser ablation have been perfected. For example, laser ablation technique has been used to produce films of uniform local stoichiometry and uniformly smooth morphology [10]. VN experiences crystal structure transformation when atoms are trapped under localized minima potential energy. Upon cooling of bulk polycrystalline VN, a cubic tetragonal phase transition occurs [11]. Hence, a theoretical explanation is required to understand its strange properties and why it is a good candidate as semiconductors or superconductors.

The heat flow theories across the layers of the products of VN are of paramount interest because of its recent superconducting features. Recent discussions on the multi-scale heat flow analysis are termed as key towards determining the heat transfer density of materials. For

✉ Moses Eterigho Emeteri
emeteri@yahoo.com;
moses.emeteri@covenantuniversity.edu.ng

¹ Department of Physics, Covenant University, Canaan Land, P.M.B 1023, Ota, Nigeria

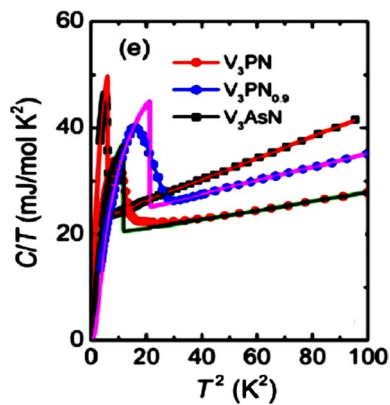
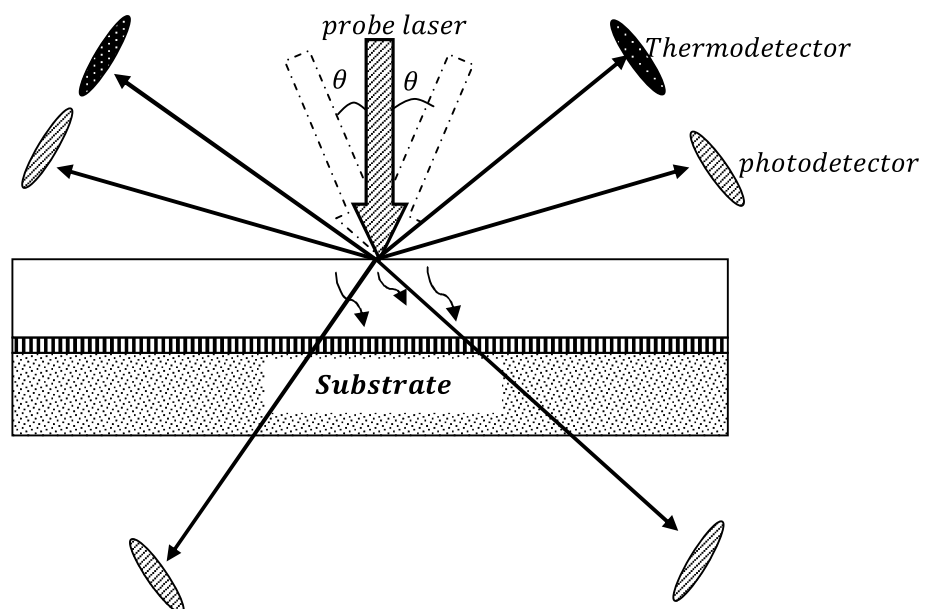


Fig. 1 Thermal properties of doped VN. Ref. [3]

example, the Constructal Theory was used to determine the dynamics of the forced convective cooling systems [12]. In this paper, we intend cooling the superconducting product of the VN to observe its cooling thermal profile. Many researchers had discussed forced convective cooling technique. Hajmohammadi et al. [13] suggested introduction of a conducting thick plate to a convective interface between the heat source and the cooling fluid. The conducting thick plate controls the excessive effect of the uniform heat flux distribution over the seemingly disordered structure below the plate. This effect has been noticed in the formation of disordered structure when vanadium nitride metallic grains were dispersed in the insulating SiO_2 matrix. Hence, the shape of the conducting thick plate is important. The Phi and Psi shaped plate had been discovered to be more efficient than the X-shaped or rectangular plate [14]. In this paper, the vanadium nitride was investigated using the probe laser

Fig. 2 Experimental set-up for measuring thermal and optical distribution



to estimate the thermal emission signals on the basis of Planck's blackbody radiation intensity distribution law. The theory of the forced convective cooling system was adopted to capture the cooling profile of the superconducting products of VN. In Sect. 2, the virtual experimentation was discussed. In Sect. 3, the formalism of theories to capture the physics of the probe laser was propounded. The application of the laser theories was executed and analyzed in Sect. 4.

2 Virtual experimentation

The superconducting sample is made-up of silicon (Si) and V^{3+} film that might be fabricated via low pressure chemical vapor deposition. A pulse KrF excimer laser (which is in its femtoseconds pulses) anneals both films at specific laser energy densities. The temperature profiling of the superconducting sample is measured by the thermal signals using thermo-detector while the photo detector measures the back-scattered light, reflectivity and transmissivity (as shown in Fig. 2). Examining the physics of the pulse KrF excimer laser, it works on Planck's black body radiation intensity distribution law.

3 Formalism

Planck's blackbody radiation intensity distribution law is used to estimate the transient temperature by the thermal emission signals from the detector. Hatano et al. [7] gave the mathematical expression of the emission signals collected by the detector as

$$V_e(T) = \frac{R_\Omega A}{\pi} \int_{\lambda_1}^{\lambda_2} \int_{\phi_1}^{\phi_2} \int_{\theta_1}^{\theta_2} \varepsilon_\lambda^t(\lambda, \theta, \phi, T) \tau(\lambda) G(\lambda) e_{\lambda b}(\lambda, T) \cos \theta \sin \theta d\theta d\phi d\lambda \tag{1}$$

where T is the temperature, θ and ϕ are the polar and azimuthal angles, λ is the wavelength, R_Ω is the impedance of the oscilloscope (50 V), A is the area on the sample which is sensed by the detector, $\varepsilon_\lambda^t(\lambda, \theta, \phi, T)$ is the spectral directional emissivity, $\tau(\lambda)$ is the transmissivity of the two lenses, $G(\lambda)$ is the responsivity (A/W) of the detector at different wavelengths, $e_{\lambda b}(\lambda, T)$ is the blackbody emissive power given as

$$e_{\lambda b} = \frac{2\pi C_1}{\lambda^5} \frac{1}{\exp(C_2/\lambda T) - 1} \tag{2}$$

$C_1 = 5.9555 \times 10^7 \text{ W } \mu\text{m}^4/\text{m}^2$, and $C_2 = 1.4388 \times 10^4 \text{ K } \mu\text{m}$.

Equation (1) is further analyzed using the separation variable technique which reduce the whole equation to

$$V_e(T) = \frac{R_\Omega A}{\pi} Y(\lambda, T) J(\theta) K(\phi) \tag{3}$$

where

$$\left. \begin{aligned} Y(\lambda, T) &= \int_{\lambda_1}^{\lambda_2} \varepsilon_\lambda^t(\lambda, T) \tau(\lambda) G(\lambda) e_{\lambda b}(\lambda, T) \\ J(\theta) &= \int_{\theta_1}^{\theta_2} \varepsilon_\lambda^t(\theta) \cos \theta \sin \theta d\theta \\ K(\phi) &= \int_{\phi_1}^{\phi_2} \varepsilon_\lambda^t(\phi) d\phi \end{aligned} \right\} \tag{4}$$

$Y(\lambda, T)$ represents the optical and thermal function which explains the first-order transition from an insulator to a metal of both the silicon and vanadium oxide. Further expansion of the $Y(\lambda, T)$ confirms experimental results of thermal characterization of individual elements i.e. silicon and vanadium. $J(\theta)$ represents the optical transport of the combined multilayered material.

$\frac{R_\Omega A}{\pi} K(\phi)$ is the charge transport which expresses the electrical characterization of the first-order transition from insulator to metal and then to superconductors. For the purpose of this paper, the thermal characterization in Eq. (4) is expressed in Fig. 3.

4 Thermal transmission

The chemical reaction reported in the virtual experiment is said to be homogeneous because at the interface, the reaction rate depends on the concentration of the species itself i.e. the silicon and vanadium. Moreso, the reaction is of the first order because the rate of reaction is directly proportional to elemental concentration [15–18].

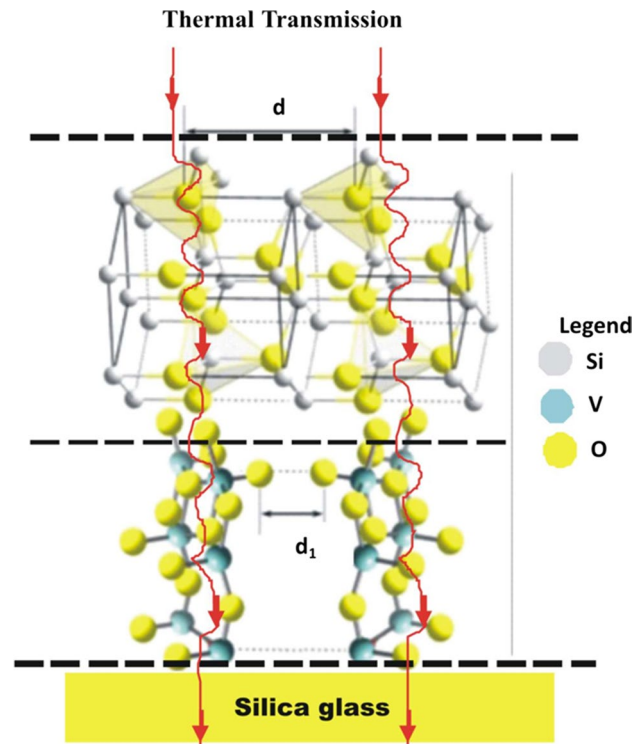


Fig. 3 Thermal transmission of KrF excimer laser

$$Y(\lambda) = \chi(T) \int_{\lambda_1}^{\lambda_2} \varepsilon_\lambda^t(\lambda) \tau(\lambda) G(\lambda) e_{\lambda b}(\lambda) \tag{5}$$

The objective of this paper is hinged on Eq. (5) i.e. estimating the temperature profile which can be expressed by the formulation of the governing equations used for the unsteady heat flow. The assumptions made includes: the emissivity of the KrF excimer laser depends on the elemental concentration; the two lenses operates at perfect functionality i.e. $\tau(\lambda) \approx 1$ and $G(\lambda) \approx 1$. The unsteady thermal transport which expresses the temperature from the air through the superconducting layers to the silica glass is expressed in Eqs. (6–8).

$$\frac{\partial Y}{\partial \lambda} = \chi(T - T_\infty) \varepsilon_\lambda^t(C - C_\infty) \tag{6}$$

$$\rho C_p \frac{\partial T}{\partial t} = k \frac{\partial^2 T}{\partial \lambda^2} \tag{7}$$

$$\frac{\partial C}{\partial t} = D \frac{\partial^2 C}{\partial \lambda^2} \tag{8}$$

C_p is the specific heat of at constant pressure ($\text{J kg}^{-1} \text{K}^{-1}$), C is the species concentration in the fluid/solid (kg m^{-3}), k is the thermal conductivity ($\text{W m}^{-1} \text{K}^{-1}$), T is the temperature profile (K), D is the mass diffusion coefficient ($\text{m}^2 \text{s}^{-1}$),

Table 1 Values of material parameters

Materials	SiO ₂	V ₂ O ₃	Silica glass
Refractive index	1.456	1.5763	1.47
Absorption coefficient (1/m)	141.726	27.50	1 × 10 ⁴
Specific heat (J/kg K)	841	0.485	703
Thermal conductivity (W/mK)	1.19	30.7	1.3
Density (kg/m ³)	2500	6110	2200

t is the time (s), $\chi(T)$ is the equivalent parameter of coefficient of expansion with concentration (0.13 % K⁻¹). ρ is the density of the material (kg m⁻³).

The initial and boundary conditions are

$$\begin{aligned}
 Y = 0, & \quad T = T_\infty, & C = C_\infty, & \text{for all } \lambda, t \leq 0 \\
 Y = Y_0 \exp(at), & T = T_\infty + T_c, & C = C_\infty + C_c, & \lambda = 0, t > 0 \\
 Y \rightarrow 0, & T \rightarrow T_\infty, & C \rightarrow C_\infty, & \lambda \rightarrow \infty
 \end{aligned}$$

The initial boundary shown above is expected to illustrate the crucial order-parameter phase of the two dissimilar films via the application of the anti-Stokes fluorescence for superconducting material [19]. The resolution of Eqs. (7, 8) yields the solution as shown in Eq. (9); the resolution of Eqs. (6, 7) yields the solution as shown in Eq. (10); the resolution of Eqs. (6, 8) yields the solution as shown in Eq. (11).

$$D = \frac{k}{\rho C_p} \tag{9}$$

$$T = \exp(D\omega t) \tag{10}$$

$$C = \exp(\omega t) \tag{11}$$

where $\omega = \left(\frac{\chi(T_c)\epsilon'_2(C_c)}{Y_0 \exp(at)}\right)^2$ and a is the initial phase difference. The parameters to be used can be found in the Table 1 as shown below. Equations (9–11) would be applied to the micro porous layered material shown in Fig. 3. For individual elements within specific layers (as shown in Fig. 3), each homogeneous part with unknown interface condition is solved and its solutions is matched for temperature and heat flow continuity. The homogeneous part is divided into two according to its porosity i.e. layers in series and layers in parallel. As the object

is illuminated by the pulse laser beam from the KrF laser excimer, the temperature profile penetrates in the order of 1 μm [20]. Since the thermal transport at the tip—sample contacts consists of air, liquid and solid–solid conduction pathways.

5 Fluid layer in series

The temperature profile is analyzed in the fluid phase over the average elemental volume of the material. This operation is performed on the assumption that the thermal surface porosity is equal to the thermal porosity of the volume. This assumption enables the determination of the c-axis critical temperature T_c of the stack in its near fluid phase via probing the thermal phase where resistive state exists under negligible bias [21]. The mathematical representation of the fluid phase is given as

$$\begin{aligned}
 \varphi(\rho C_p)_f \frac{\partial T_f}{\partial t} + (\rho C_p)_f v \nabla T_f \\
 = \varphi \nabla \left(\left(\frac{\sum \delta_i}{\sum \delta_i/k_i} \right)_f \nabla T_f \right) + \varphi q_f^{III}
 \end{aligned} \tag{12}$$

Where q^{III} (W/m³) is the heat production per unit volume, φ is the ratio of the cross sectional area occupied by the fluid to the total volume of the element.

The initial and boundary conditions for all four cases i.e. fluid layer in series, fluid layer in parallel, solid layer in series and solid layer in parallel is given as

$$\begin{aligned}
 q_f^{III} = 0, \quad v = 0, \quad \varphi = 0, \quad t = 0 \\
 q_f^{III} \ll 1, \quad v = v_i, \quad \varphi = \varphi_\infty, \quad t > 0 \\
 q_f^{III} \rightarrow 0, \quad v \rightarrow v_i, \quad \varphi \rightarrow \varphi_\infty,
 \end{aligned}$$

Applying Eqs. (10)–(12) yields Eq. (13) and Tables 2, 3 and 4.

$$(\varphi\omega + \delta_i)k_i = \varphi \left(\frac{\sum \delta_i}{\sum \delta_i/k_i} \right) D^2 t^2 \tag{13a}$$

The ratio of the cross sectional area occupied by the fluid to the total volume of the element was varied in Table 4 to see its effects on the temperature profile.

Table 2 Parameters of a liquid layer in series ($\varphi = \frac{1}{8}$, $k_i = \frac{1.19 \text{ W}}{\text{mK}}$, $P = 0.45 \text{ W}$) for silicon oxide

δ_i (nm)	C_p (J kg ⁻¹ K ⁻¹)	D (10 ⁻⁶)	ω (10 ⁻²⁸)	ϵ'_2 (10 ⁻⁶)	C (kg m ⁻³)	T (K)
50	841	0.5660	0.1767	0.5821	–83.7100	174.9055
45	853	0.5580	0.1718	0.5739	–83.7382	174.8631
40	867	0.5490	0.1663	0.5646	–83.7709	174.8139
35	874	0.5446	0.1636	0.5601	–83.7869	174.7899
30	881	0.5403	0.1610	0.5557	–83.8029	174.7659
25	894	0.5324	0.1564	0.5476	–83.8321	174.7222

Table 3 Parameters of a liquid layer in series ($\varphi = \frac{1}{8}$, $k_i = \frac{30.7 \text{ W}}{\text{mK}}$, $P = 0.45 \text{ W}$) for vanadium oxide

δ_i (nm)	C_p (J kg ⁻¹ K ⁻¹)	D	ω (10 ⁻²³)	ε_2^t (10 ⁻³)	C (kg m ⁻³)	T (K)
50	0.485	0.0104	0.8897	0.4130	-70.5808	197.8493
45	0.501	0.0100	0.8337	0.3998	-70.6458	197.7519
40	0.585	0.0086	0.6115	0.3424	-70.9555	197.2870
35	0.621	0.0081	0.5427	0.3225	-71.0749	197.1082
30	0.677	0.0074	0.4566	0.2959	-71.2482	196.8486
25	0.721	0.0070	0.4026	0.2778	-71.3742	196.6594

Table 4 Parameters of a liquid layer in series ($\varphi = \frac{1}{16}$, $k_i = \frac{30.7 \text{ W}}{\text{mK}}$, $P = 0.45 \text{ W}$) for vanadium oxide

δ_i (nm)	C_p (J kg ⁻¹ K ⁻¹)	D	ω (10 ⁻²³)	ε_2^t (10 ⁻³)	C (kg m ⁻³)	T (K)
50	0.485	0.0104	0.4448	0.2920	-71.2740	197.1562
45	0.501	0.0100	0.4169	0.2827	-71.3390	197.0587
40	0.585	0.0086	0.3057	0.2421	-71.6493	196.5946
35	0.621	0.0081	0.2713	0.2281	-71.7687	196.4150
30	0.677	0.0074	0.2283	0.2092	-71.9405	196.1567
25	0.721	0.0070	0.2013	0.1964	-72.0673	195.9677

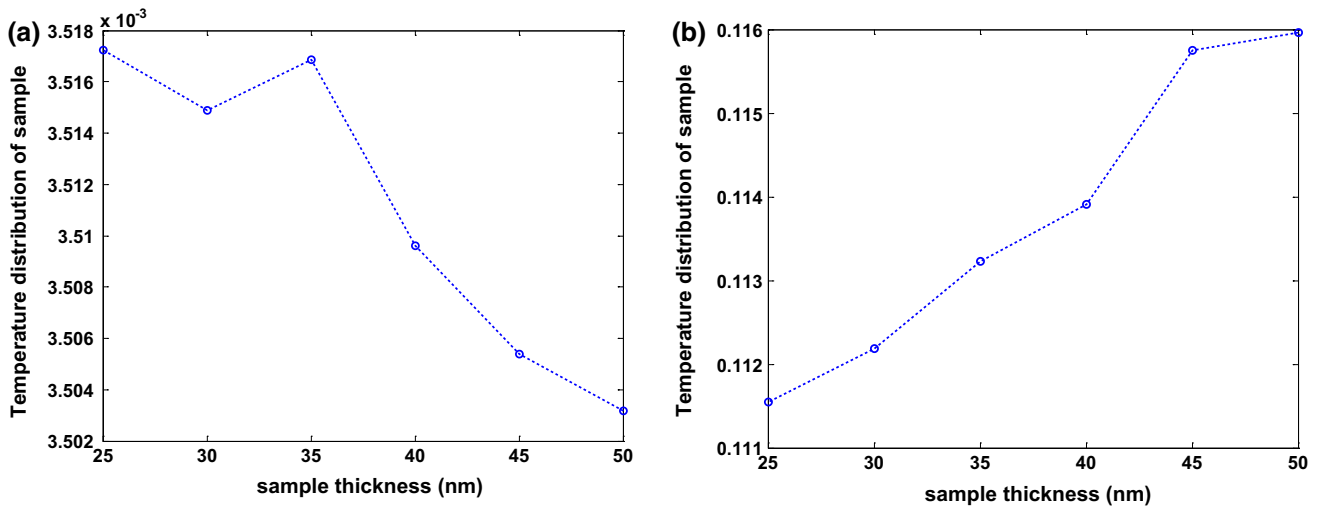


Fig. 4 **a** Temperature distribution of heterogeneous reaction; **b** Temperature distribution of homogeneous reaction

The physics of the temperature distribution in series fluid layer is further expanded by the mesh theory [13] where

$$\left| \left(\theta^i - \theta^{i-1} \right) / \theta^i \right| < 10^{-1} \tag{13b}$$

In Fig. 4a, θ^i is the temperature calculated using $\varphi = \frac{1}{8}$ and $k_i = \frac{30.7 \text{ W}}{\text{mK}}$, while θ^{i-1} is the temperature calculated using $\varphi = \frac{1}{16}$ and $k_i = \frac{30.7 \text{ W}}{\text{mK}}$. In Fig. 4b, θ^i is the temperature calculated using $\varphi = \frac{1}{8}$ and $k_i = \frac{30.7 \text{ W}}{\text{mK}}$, while θ^{i-1} is the temperature calculated using $\varphi = \frac{1}{8}$ and $k_i = \frac{1.19 \text{ W}}{\text{mK}}$.

6 Solid layer in series

The temperature profile is also analyzed in the solid phase of average elemental volume of the material. Like the fluid

layer, the assumption that the thermal surface porosity is equal to the thermal porosity of the volume still holds. The mathematical representation of the solid phase is given as

$$(1 - \varphi)(\rho C_p)_s \frac{\partial T_s}{\partial t} = (1 - \varphi)(\rho C_p)_s \nabla \cdot \left(\left(\frac{\sum \delta_i}{\sum \delta_i / k_i} \right)_s \nabla T_s \right) + (1 - \varphi)q_s^{III} \tag{14}$$

where q_s^{III} (W/m³) is the heat production per unit volume, φ is the ratio of the cross sectional area occupied by the fluid to the total volume of the element.

Applying Eqs. (10)–(14) yields Eq. (15) and Tables 5 and 6

$$\omega = \left(\frac{\sum \delta_i}{\sum \delta_i / k_i} \right) \frac{D^2 \tau^2}{k_i} \tag{15}$$

Table 5 Parameters of a liquid layer in series ($\varphi = \frac{1}{8}$, $k_i = \frac{1.19 \text{ W}}{\text{mK}}$, $P = 0.45 \text{ W}$) for silicon oxide

δ_i (nm)	C_p (J kg ⁻¹ K ⁻¹)	D (10 ⁻⁶)	ω (10 ⁻²⁷)	ε'_λ (10 ⁻⁵)	C (kg m ⁻³)	T (K)
50	841	0.5660	0.2002	0.1959	-81.2826	177.3328
45	853	0.5580	0.1946	0.1932	-81.3108	177.2902
40	867	0.5490	0.1884	0.1900	-81.3434	177.2415
35	874	0.5446	0.1854	0.1885	-81.3594	177.2173
30	881	0.5403	0.1824	0.1870	-81.3755	177.1932
25	894	0.5324	0.1772	0.1843	-81.4047	177.1492

Table 6 Parameters of a liquid layer in series ($\varphi = \frac{1}{8}$, $k_i = \frac{30.7 \text{ W}}{\text{mK}}$, $P = 0.45 \text{ W}$) for vanadium oxide

δ_i (nm)	C_p (J kg ⁻¹ K ⁻¹)	D	ω (10 ⁻¹⁹)	ε'_λ	C (kg m ⁻³)	T (K)
50	0.485	0.0104	0.6708	0.0359	-61.6528	206.7772
45	0.501	0.0100	0.6286	0.0347	-61.7174	206.6799
40	0.585	0.0086	0.4611	0.0297	-62.0274	206.2150
35	0.621	0.0081	0.4092	0.0280	-62.1471	206.0363
30	0.677	0.0074	0.3443	0.0257	-62.3195	205.7772
25	0.721	0.0070	0.3035	0.0241	-62.4456	205.5883

Table 7 Parameters of a liquid layer in parallel ($\varphi = \frac{1}{8}$, $k_i = \frac{1.19 \text{ W}}{\text{mK}}$, $P = 0.45 \text{ W}$) for silicon oxide

δ_i (nm)	C_p (J kg ⁻¹ K ⁻¹)	D (10 ⁻⁶)	$\varphi\omega$ (10 ⁻²⁷)	ε'_λ (10 ⁻⁵)	C (kg m ⁻³)	T (K)
50	841	0.5660	0.2002	0.1959	-81.2826	177.3328
45	853	0.5580	0.1946	0.1932	-81.3108	177.2902
40	867	0.5490	0.1884	0.1900	-81.3434	177.2415
35	874	0.5446	0.1854	0.1885	-81.3594	177.2173
30	881	0.5403	0.1824	0.1870	-81.3755	177.1932
25	894	0.5324	0.1772	0.1843	-81.4047	177.1492

Table 8 Parameters of a liquid layer in parallel ($\varphi = \frac{1}{8}$, $k_i = \frac{30.7 \text{ W}}{\text{mK}}$, $P = 0.45 \text{ W}$) for vanadium oxide

δ_i (nm)	C_p (J kg ⁻¹ K ⁻¹)	D	ω (10 ⁻¹⁹)	ε'_λ	C (kg m ⁻³)	T (K)
50	0.485	0.0104	0.6708	0.0359	-61.6528	206.7772
45	0.501	0.0100	0.6286	0.0347	-61.7174	206.6799
40	0.585	0.0086	0.4611	0.0297	-62.0274	206.2150
35	0.621	0.0081	0.4092	0.0280	-62.1471	206.0363
30	0.677	0.0074	0.3443	0.0257	-62.3195	205.7772
25	0.721	0.0070	0.3035	0.0241	-62.4456	205.5883

7 Liquid layer in parallel

Like the Layers in series, the temperature profile is analyzed in the fluid phase of the averages over elemental volume of the material. The mathematical representation of the fluid phase is given as

$$\varphi(\rho C_p)_f \frac{\partial T_f}{\partial t} + (\rho C_p)_f v \nabla T_f = \varphi \nabla \left(\left(\frac{\sum \delta_i k_i}{\sum \delta_i} \right)_f \nabla T_f \right) + \varphi q_f''' \tag{16}$$

where q_f''' (W/m³) is the heat production per unit volume, φ is the ratio of the cross sectional area occupied by the fluid to the total volume of the element.

Applying Eqs. (10)–(16) yields Eq. (17) and Tables 7 and 8

$$(\varphi\omega + \delta_i)k_i = \varphi \left(\frac{\sum \delta_i k_i}{\sum \delta_i} \right) D^2 t^2 \tag{17}$$

8 Solid layer in parallel

The temperature profile is analyzed in the solid phase (under the parallel arrangement of porosity) over the average elemental volume of the material. Like the fluid layer, we worked on the assumption that the thermal surface porosity is equal to the thermal porosity of the volume. The mathematical representation of the solid phase is given as

Table 9 Parameters of a solid layer in parallel ($\varphi = \frac{1}{8}$, $k_i = \frac{1.19 \text{ W}}{\text{mK}}$, $P = 0.45 \text{ W}$) for silicon oxide

δ_i (nm)	C_p (J kg ⁻¹ K ⁻¹)	D (10 ⁻⁶)	ω (10 ⁻²⁷)	ε'_λ (10 ⁻⁵)	C (kg m ⁻³)	T (K)
50	841	0.5660	0.2002	0.1959	-81.2826	177.3328
45	853	0.5580	0.1946	0.1932	-81.3108	177.2902
40	867	0.5490	0.1884	0.1900	-81.3434	177.2415
35	874	0.5446	0.1854	0.1885	-81.3594	177.2173
30	881	0.5403	0.1824	0.1870	-81.3755	177.1932
25	894	0.5324	0.1772	0.1843	-81.4047	177.1492

Table 10 Parameters of a solid layer in parallel ($\varphi = \frac{1}{8}$, $k_i = \frac{30.7 \text{ W}}{\text{mK}}$, $P = 0.45 \text{ W}$) for vanadium oxide

δ_i (nm)	C_p (J kg ⁻¹ K ⁻¹)	D	ω (10 ⁻¹⁹)	ε'_λ	C (kg m ⁻³)	T (K)
50	0.485	0.0104	0.6708	0.0359	-61.6528	206.7772
45	0.501	0.0100	0.6286	0.0347	-61.7174	206.6799
40	0.585	0.0086	0.4611	0.0297	-62.0274	206.2150
35	0.621	0.0081	0.4092	0.0280	-62.1471	206.0363
30	0.677	0.0074	0.3443	0.0257	-62.3195	205.7772
25	0.721	0.0070	0.3035	0.0241	-62.4456	205.5883

Table 11 Parameters of a solid layer in parallel ($\varphi = \frac{1}{8}$, $k_i = \frac{30.7 \text{ W}}{\text{mK}}$, $P = 0.45 \text{ W}$) for silica glass

δ_i (nm)	C_p (J kg ⁻¹ K ⁻¹)	D (10 ⁻⁶)	ω (10 ⁻²⁷)	ε'_λ (10 ⁻⁵)	C (kg m ⁻³)	T (K)
50	703	0.8406	0.4416	0.2910	-80.4915	178.5192
45	707	0.8358	0.4366	0.2893	-80.5034	178.5022
40	715	0.8264	0.4269	0.2861	-80.5256	178.4684
35	722	0.8184	0.4186	0.2833	-80.5445	178.4392
30	729	0.8106	0.4106	0.2806	-80.5638	178.4102
25	734	0.8051	0.4051	0.2787	-80.5776	178.3898

$$(1 - \varphi)(\rho C_p)_s \frac{\partial T_s}{\partial t} = (1 - \varphi)(\rho C_p)_s \nabla \cdot \left(\left(\frac{\sum \delta_i k_i}{\sum \delta_i} \right)_s \nabla T_s \right) + (1 - \varphi) q_s^{III} \quad (18)$$

where q^{III} (W/m³) is the heat production per unit volume, φ is the ratio of the cross sectional area occupied by the fluid to the total volume of the element.

Applying Eqs. (10)–(14) yields Eq. (15) and Tables 5 and 6

$$\omega = \left(\frac{\sum \delta_i k_i}{\sum \delta_i} \right) \frac{D^2 t^2}{k_i} \quad (19)$$

In Fig. 4a, θ^i is the temperature calculated using $\varphi = \frac{1}{8}$ and $k_i = \frac{30.7 \text{ W}}{\text{mK}}$, while θ^{i-1} is the temperature calculated using $\varphi = \frac{1}{8}$ and $k_i = \frac{30.7 \text{ W}}{\text{mK}}$. In Fig. 4b, θ^i is the temperature calculated using $\varphi = \frac{1}{8}$ and $k_i = \frac{30.7 \text{ W}}{\text{mK}}$ for vanadium film, while θ^{i-1} is the temperature calculated using $\varphi = \frac{1}{8}$ and $k_i = \frac{30.7 \text{ W}}{\text{mK}}$ for silicon film (Tables 9, 10, 11).

9 Results and discussion

From the cooling thermal profiles of vanadium concentration, material thickness and temperature, it is

concluded that the superconducting VN satisfied current superconducting thermal range i.e. the critical temperature do not exceed the room temperature [22, 23]. The temperature distributions are examined under an irradiating laser intensity of 0.45 W, pulse energies of 200–1100 mJ, wavelength of 248 nm, ablation fluencies range of 0.3 and 30 J cm⁻². The temperature distribution in fluid layer in series (Fig. 4a, b) was investigated via the mesh theory. The fluid phase of the vanadium and silicon films (Fig. 4a) follows a negative trend which affirms the incompatibility of the heterogeneous reaction [24]. The compatibility of vanadium film at its fluid in series phase affirmed its compatibility even at varying k_i . The effective decay rate probability density function [25] which is peculiar to photoluminescence decay was exhibited as elements relax into equilibrium (see Fig. 6). When the ultrashort KrF excimer laser pulse drives the system out of equilibrium, the response of the correlated electronic system when silicon is at the topmost layer (for both the layer in series and in parallel) experiences an initial modulation and then demodulates to attain equilibrium while the vanadium at the topmost layer (for both the layer in series and in parallel) experiences an initial demodulation until it attains

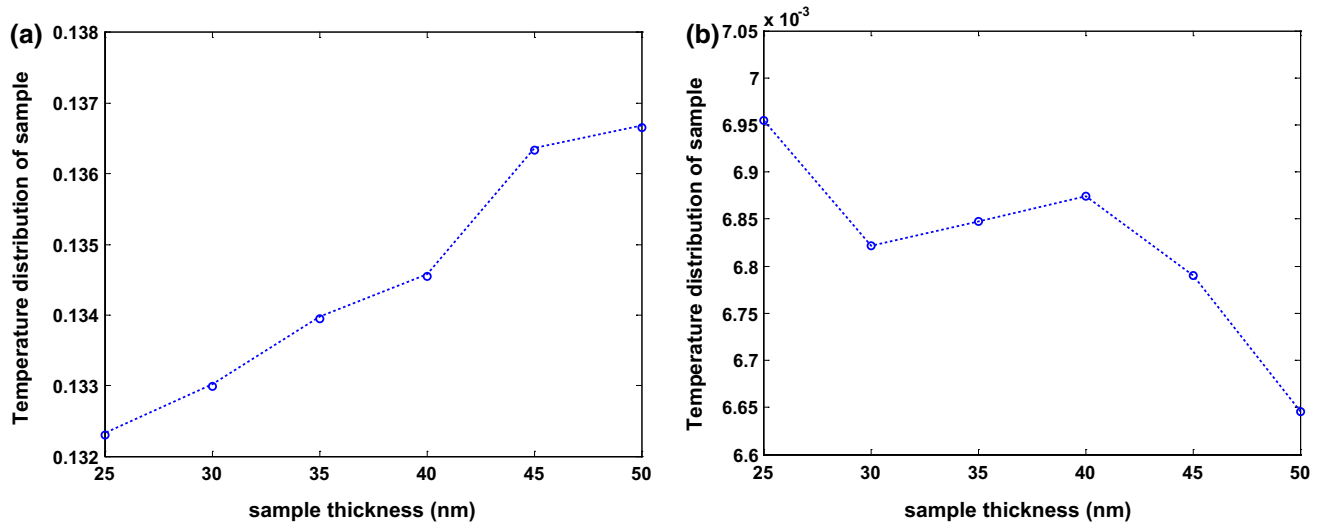


Fig. 5 **a** Temperature distribution of heterogeneous reaction; **b** Temperature distribution of homogeneous reaction

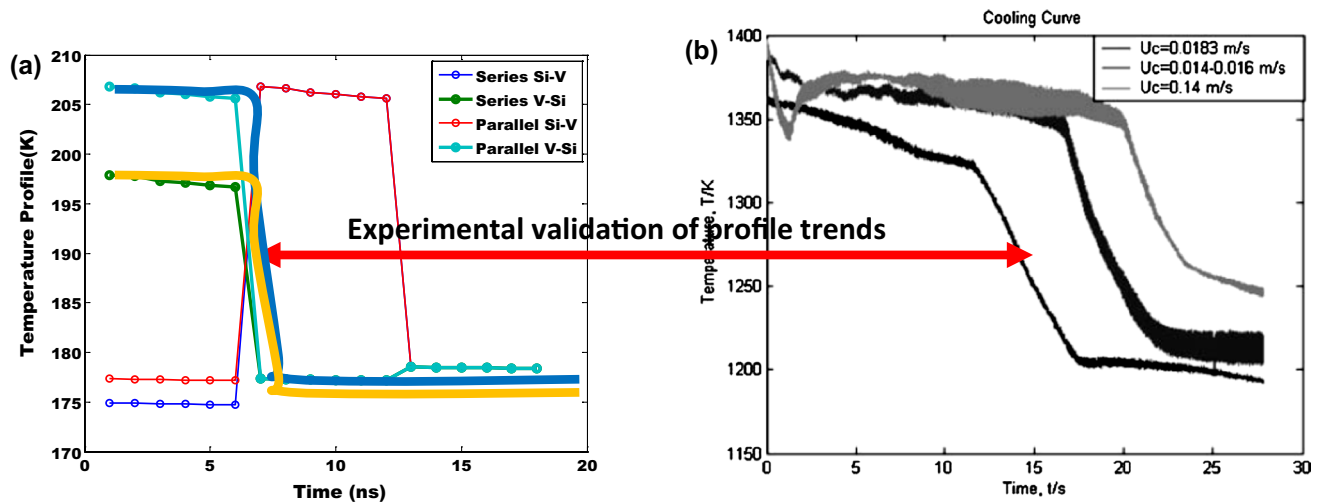


Fig. 6 **a** Theoretical trends of Temperature profiles in series solidification. **b** Experimental trends of Temperature profiles in series solidification Mahmoudi et al. [29]

equilibrium. This shows the importance of stoichiometry and characteristic effects on preferential reaction of the silicon and vanadium to achieve microelectronic results. The possible critical temperatures of the interlayer were shown to be 188 and 192 K. Previous experiments on the silicon-vanadium material (nano-materials) show a critical temperature of 145 K [26]. Though the temperature distribution of the cooling system was found to align with the experimental results [27], Fig. 5a revealed that the homogenous reaction between silicon film and glass are not compatible during solidification along the parallel phase. However, the heterogeneous reaction between the vanadium and silicon film

is compatible (see Fig. 5b). Further on the heterogeneous metallic compound, Fig. 6 affirmed it's correctness-experimentally. For example, the model was able to capture the temperature profiles of a plateau cooling curve (from centerline jets of an experimental work). At the plateau, the temperature (known as the solidification temperature) is almost constant. Other known features like sudden change in the slope of the curve attest to the validation of our model. In other words, the dynamics of the electronic structure of the thermally-excited materials is hinged on the complementary stoichiometry signatures, thermal properties amongst others. Also, $V_2O_3-SiO_2$ compounds are more efficient in the series

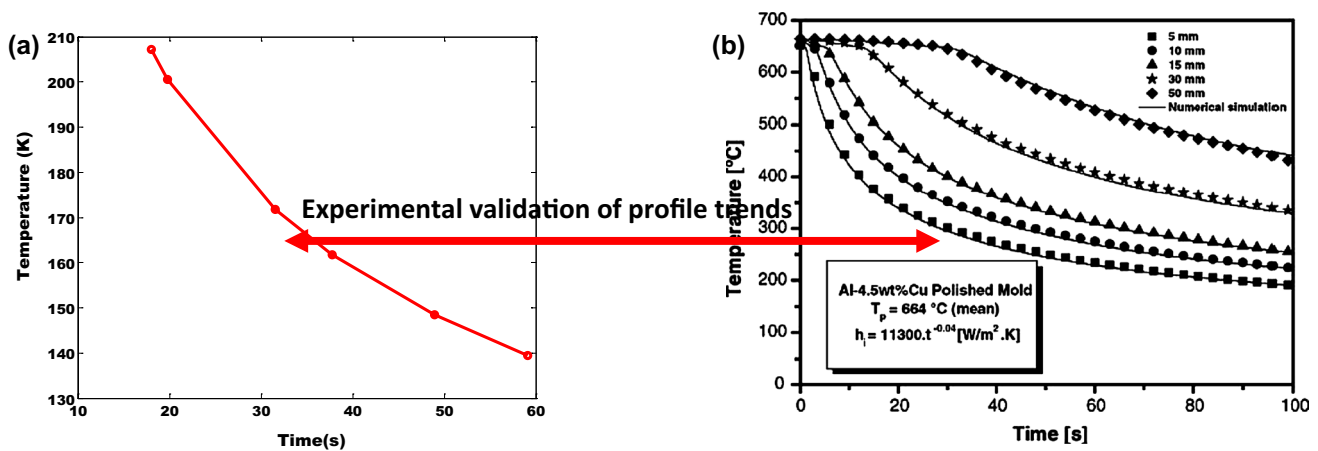


Fig. 7 **a** Theoretical trends of Temperature profiles in series solidification. **b** Experimental trends of Temperature profiles in series solidification Ferreira et al. [30]

type of layering. Series types of layering are the most viable options to improve the conductivity of heterogeneous metallic compounds. It also help to reduce the localization of electron–hole to site in semiconductors [28] etc. Also, we further investigated the characteristic temperature profile within each layers in series. It was also validated experimentally [30] hence, the thermophysical properties of alloy i.e. its solidification process is upward as shown in the Fig. 7. These results affirm the idea of stacking the building blocks of VN to manipulate its electrical property and electronic structure [11].

10 Conclusion

The in-depth analysis of the fluid phase in series and parallel, as well as the solid phase in series and parallel has affirmed that this idea can be used to implement parametric cooling in superconducting materials. The operation parameters of the KrF excimer laser adopted for this study enables the material to exhibit the effective decay rate probability density function which is peculiar to the photoluminescence decay. This makes VN a good candidate for semiconductor technology. Hence, the dynamics of the electronic structure of the thermally-excited VN products is hinged on the complementary stoichiometry signatures, thermal properties amongst others. The temperature distribution of the cooling system of VN products was found to align with experimental results. It also revealed that the homogenous reaction between silicon film and glass are not compatible during solidification along the parallel phase. The maximum possible critical temperatures of the inter-layer were calculated to be about 206 K.

Acknowledgments The paper enjoys the partial sponsorship of Covenant University.

References

1. Qazilbash M, Brehm M, Chae B et al (2007) Mott transition in VO₂ revealed by infrared spectroscopy and nano-imaging. *Science* 318:5857
2. Im JS, Sposili RS (1996) Crystalline Si films for integrated active-matrix liquid-crystal displays. *Mater Res Bull* 21:39
3. Wang B, Ohgushi K (2013) Superconductivity in anti-post-perovskite vanadium compounds. *Sci Rep* 3:3381
4. Koscielska B, Yuzepovich OI, Bengus SV, Winiarski A, Sadowski W, Lapinski M (2012) Polaritonic microwave waves of inclined incidence in some magnetodielectric superlattices. *Acta Phys Polonica* 122(5):833–836
5. Nebel G, Christiansen S, Strunk H, Stutzmann M (1998) Laser-interference crystallization of amorphous silicon: applications and properties. *Phys Status Solidi A* 166:667
6. Ishihara R, Matsumura M (1998) Excimer-laser produced single-crystal Si thin film transistors. *Jpn J Appl Phys* 36:6167
7. Hatano M, Moon S, Lee M (2000) Excimer laser-induced temperature field in melting and resolidification of silicon thin films. *J Appl Phys* 87:36–43
8. Gaponov SV, Luskin BM, Nesterov BA, Salaschenko NN (1978) Low temperature epitaxy of films condensed from a laser produced plasma. *Sov Phys Solid State* 19:1736
9. Ong NP, Kote G, Cheung JT (1983) Logarithmic behavior in a new two-dimensional metal: HgTe-CdTe superlattice. *Phys Rev B* 28:2289
10. Lowndes DH, Geohegan DB, Eres D, Pennycook SJ, Mashburn DN, Jellison GE (1988) Photon-controlled fabrication of amorphous superlattice structures using ArF (193 nm) excimer laser photolysis. *Appl Phys Lett* 52(22):1868–1870
11. Mei AB, Hellman O, Wireklint N, Schlepütz CM, Sangiovanni DG, Alling B, Rockett A, Hultman L, Petrov I, Greene JE (2015) Dynamic and structural stability of cubic vanadium nitride. *Phys Rev B* 91:054101
12. Bejan A, Sciubba E (1992) The optimal spacing for parallel plates cooled by forced convection. *Int J Heat Mass Transf* 35:3259–3264
13. Hajmohammadi MR, Salimpour MR, Saber M, Campo A (2013) Detailed analysis for the cooling performance enhancement of a heat source under a thick plate. *Energy Convers Manag* 76:691–700

14. Hajmohammadi MR, Shariatzadeh OJ, Moulod M, Nourazar SS (2014) Phi and Psi shaped conductive routes for improved cooling in a heat generating piece. *Int J Thermal Sci* 77:66–74
15. Emeteri ME (2014) Analytical temperature profiling for pipe walls and fluids using mathematical experimentation. *Adv. Mech. Eng.* 2014:490302
16. Chambre PL, Young JD (1958) On the diffusion of a chemically reactive species in a laminar boundary layer flow. *Phys Fluids* 1:48–54
17. Das UN, Deka RK, Soundalgekar VM (1999) Effect of mass transfer on flow past an impulsively started infinite vertical plate with chemical reaction. *Bull GUMA* 5:13–20
18. Muthucumaraswamy R, Sundar Raj M, Subramanian VSA (2009) Exact solution of flow past an accelerated infinite vertical plate with heat and mass flux. *Int J Appl Mech Eng* 14:585–592
19. Nemova G, Kashyap R (2010) Laser cooling of solids. *Rep Prog Phys* 73:086501
20. Grigoropoulos P, Park HK, Xu X (1993) Modeling of pulsed laser irradiation of thin silicon layers. *Int J Heat Mass Transfer* 36:919–924
21. Machida M, Sakai S (2004) Unified theory for magnetic and electric field coupling in multistacked Josephson junctions. *Phys Rev B* 70:144520
22. Uno UE, Emeteri ME (2011) Isotope effect on cuprates component in determining experimental critical temperature. *Int J Sci Res* 1:15–24
23. Uno UE, Emeteri ME (2012) Analysis of the high temperature superconducting magnetic penetration depth using the Bloch NMR equations. *Glob Eng Technol Rev* 2:14–21
24. Koscielska B, Yuzepovich OI, Bengus SV, Winiarski A, Sadowski W, Lapinski M (2012) Superconducting properties of VN₂SiO₂ Sol_Gel derived thin films. *Acta Phys Pol, A* 121:832–836
25. Emeteri ME (2013) Modeling the non-single exponential photoluminescence decay using the boubaker polynomial expansion scheme. *J Adv Phys* 2:213–215
26. Werthamer NR, Helfand E, Hohenberg PC (1966) Temperature and purity dependence of the superconducting critical field, H_{c2}. III. Electron spin and spin-orbit effects. *Phys Rev* 147:295–302
27. Collier JG, Thome JR (1996) Convective boiling and condensation, 3rd edn. Oxford University Press, Oxford, pp 217–349
28. Uno UE, Emeteri ME, Isah KU, Ahmadu U (2012) On the effect of electron-hole recombination in disordered GaAs-AA1-XAlAs multi-quantum well structure. *Int J Fundam Phys Sci* 3:35–40
29. Mahmoudi J, Vynnycky M, Sivesson P, Fredriksson H (2003) An experimental and numerical study on the modelling of fluid flow, heat transfer and solidification in a copper continuous strip casting process. *Mater Trans* 44:1741–1751
30. Ferreira IL, Spinelli JE, Pires JC, Garci A (2005) The effect of melt temperature profile on the transient metal/mold heat transfer coefficient during solidification. *Mater Sci Eng A* 408:317–325